This is a preprint, the final version is subject to change, of the American Mineralogist (MSA)
Cite as Authors (Year) Title. American Mineralogist, in press.
(DOI will not work until issue is live.) DOI: http://dx.doi.org/10.2138/am.2014.4735

EXPERIMENTAL DETERMINATION OF MELTING IN THE SYSTEMS ENSTATITE-MAGNESITE AND MAGNESITE-CALCITE FROM 15 TO 80 GPA

Revision 1

A.R. THOMSON[a]*, M.J. WALTER[a], O.T. Lord[a,b], S.C. KOHN[a].

[a]School of Earth Sciences, University of Bristol, Wills Memorial Building, Queens's Road, Bristol, BS8 2HX.

[b]Department of Earth Sciences, University College London, Gower Street, London, WC1E 6BT, UK

*Corresponding Author

Email: andrew.thomson@bristol.ac.uk

Phone: +44 117 3315196

ABSTRACT

Pressure-temperature melting curves in two carbonate bearing systems of relevance to Earth's mantle have been determined using the laser-heated diamond anvil cell (LH-DAC). The solidus along the $MgSiO_3$-$MgCO_3$ join in the MgO-SiO_2-CO_2 system (MS-CO_2) was defined from 15 to 80 GPa using *in-situ* melting criteria, reaching a maximum temperature of ~2340 K at 80 GPa. The occurrence of melting has been confirmed with *ex-situ* textural and chemical analysis of recovered samples. The melting curve has a negative dT/dP slope at pressures between ~15 and 23 GPa resulting from the subsolidus phase transition of ilmenite- to perovskite-structured $MgSiO_3$. The shallow slope of the melting curve at pressures higher than this transition indicate that for plausible mantle geotherms carbonate-bearing silicate lithologies will melt throughout the lower mantle. The solidus of a mixture

along the $MgCO_3$-$CaCO_3$ join was determined as a proxy for alkali-free carbonate lithologies. Melting temperatures increase from 1860 K at 16 GPa to ~ 2100K above 35 GPa, where the melting curve flattens. The melting reaction magnesite + post-aragonite (high-pressure $CaCO_3$) = melt was confirmed using an *in-situ* experiment. We conclude that crystalline Mg and Ca carbonate mixtures are unstable with respect to molten carbonate at conditions of the convective lower mantle. The flat melting curves at high pressures in both systems suggests that subducted carbonates will undergo melting at lower mantle conditions, a process that may be important for superdeep diamond formation and carbon storage in the deep mantle.

Keywords: deep carbon, diamond anvil cell, magnesite, melting

1. INTRODUCTION

Carbon is a key component of Earth's atmosphere and biosphere and is essential for the preservation of a habitable climate throughout geological time. The atmospheric carbon budget is maintained by exchange with mantle reservoirs through subducting material and volcanic degassing (Sleep and Zhanle, 2001). The overall mantle carbon budget is not well constrained due to uncertainties in the primary bulk earth carbon budget and incoming/outgoing fluxes, but its massive size makes it a large potential carbon storage reservoir (Dasgupta and Hirschmann, 2010). Hirschmann and Dasgupta (2009) estimate that the H/C ratio of the mantle is superchondritic, an observation inconsistent with a chondritic Earth or one where the late veneer dominates the volatile budget, and the presence of a hidden carbon-rich reservoir in the deep Earth is one possible explanation. The fate of subducted carbon has been the subject of many studies in recent decades, and its presence can have large effects on the chemical, physical and redox behaviour of the mantle (Frost and McCammon 2008; Gaillard *et*

47 *al.,* 2008; Stagno and Frost, 2010; Rohrbach and Schmidt, 2011; Walter *et al.,* 2011; Dasgupta *et al.,*
48 2013; Dasgupta, 2013; Shirey *et al.,* 2013).
49
50 The activity of oxygen is the critical factor in determining the form of carbon that exists in the mantle,
51 as it fixes the distribution of oxidised and reduced carbon species. Peridotitic mantle with constant
52 oxygen content should become more reducing with depth as a consequence of increased ferric iron
53 solubility in deep mantle phases like majorite and perovskite. There is evidence for this in samples of
54 cratonic lithosphere and some inclusions in diamonds originating in the lower mantle (McCammon et
55 al, 1997; Woodland and Koch, 2003; Frost and McCammon, 2008; Rohrbach and Schmidt, 2011).
56 However, the exact oxygen content of the majority of the mantle is not constrained by samples. The
57 redox state of carbon within slabs as they subduct into the mantle is also not well known. Initially the
58 majority of carbon introduced into the mantle is in oxidised forms, mostly carbonates added to ocean-
59 floor material during alteration by hydrothermal fluids and seawater interaction (Shilobreeva *et al.,*
60 2011). Thermodynamic models and petrological experiments indicate that carbonates can remain stable
61 in slabs as they undergo metamorphism and dehydration in the sub-arc mantle (Connolly, 2005;
62 Gorman *et al.,* 2006; Molina and Poli, 2000; Poli *et al.,* 2009), and carbonate phases are known to have
63 stability fields that extend throughout the mantle depth range (Isshiki *et al.,* 2004). There is now
64 significant tomographic and geodynamic evidence that subducting slabs can penetrate into the lower
65 mantle (van der Meer *et al.,* 2010; Steinberger *et al.,* 2012). It is therefore important to understand
66 what happens to the carbon cargo carried by slabs into the deep mantle.
67
68 Previous work on the effect of carbonate on silicate phase relations at upper mantle pressures is
69 extensive (e.g Katsura and Ito, 1990; Luth, 1993; Hammouda, 2003; Dasgupta *et al.,* 2004; Yaxley and

Brey, 2004; Kiseeva *et al.,* 2012; Keshav and Gudfinnsson, 2010; Litasov and Ohtani, 2010; Martin *et al.,* 2012; Kiseeva *et al.,* 2013). At pressures relevant to the lower mantle, the stability of carbonate minerals coexisting with mantle silicates is much more uncertain, and it is possible that decarbonation reactions, which produce free CO_2 or other carbon phases, can occur. Recent work shows that at lower mantle pressures and temperatures CO_2 should be a liquid or may even dissociate into C + O_2 (Litasov *et al.,* 2011; Boates *et al.,* 2012; Teweldeberhan *et al.,* 2013). In contrast, the stability of magnesite at 85 GPa and 3000 K (Isshiki *et al.,* 2004) suggests that the decarbonation of carbonate minerals does not occur under mantle conditions. This view is further supported by the observation that MgO and CO_2 react to form $MgCO_3$ at 5-40 GPa and 1400-1800 K (Scott *et al.,* 2013). Seto *et al.* (2008) investigated the reaction of $MgCO_3$ and SiO_2 at lower mantle pressures to address the potential decarbonation of subducting materials that contain free SiO_2. It was observed that $MgSiO_3$ and CO_2 were formed by a decarbonation reaction above ~ 2400 K from 30 – 80 GPa. However, thermodynamic modelling of this reaction was found to be inconsistent with the experimental data (Litasov *et al.,* 2008).

Carbonate suppresses the silicate solidus considerably at upper mantle conditions, so carbonated-melt is potentially the most important deep mantle carbon-bearing phase. Experimental studies on carbonated materials, both peridotitic and eclogitic, at upper mantle pressures have shown that low degree melts are carbonate-rich, often containing < 1wt.% SiO_2 (Dalton and Presnall, 1998; Hammouda, 2003; Dasgupta *et al.,* 2004; Kiseeva *et al.,* 2013 etc.). Therefore the melting temperature of all such carbonated (anhydrous) materials can be estimated from the melting curves of pure carbonate systems (Buob *et al.,* 2006, Franzolin *et al.,* 2011). The melting behaviour of simple carbonate systems is a suitable proxy for many alkali-free carbonate-bearing lithologies. For example they can be used to understand the behaviour of slab material that has undergone sub-arc melting (and

hence contains low residual concentrations of alkali components) or the melting of carbonated peridotite.

Previously, Katsura and Ito (1990) investigated the $MgSiO_3$-$MgCO_3$ binary system, observing that at 8 and 15 GPa a eutectic melt is formed at ~ 2050 – 2100 K. Despite its potential relevance throughout the mantle, this eutectic melting reaction has not been explored further. In this study we extend the melting curve to ~ 80 GPa in the $MgSiO_3$-$MgCO_3$ system using laser-heated diamond anvil cell (LH-DAC) experiments. In addition, we determine the melting curve in the system $MgCO_3$-$CaCO_3$ to ~ 80 GPa. These experiments provide new information regarding the maximum temperature stability of carbonate phases within the convecting mantle.

2. METHODS

This study consists of experiments in two separate chemical systems, $MgSiO_3$-$MgCO_3$ and $MgCO_3$-$CaCO_3$. Melting curves were determined using experiments performed in the LH-DAC at the School of Earth Sciences, University of Bristol (described in section 2.1). One subsolidus run was performed in the $MgSiO_3$-$MgCO_3$ system. Additionally a single experiment was conducted with *in-situ* X-ray diffraction (XRD) in the LH-DAC at beamline ID-27 of the European Synchrotron Radiation Facility (ESRF) in Grenoble, France (described in section 2.2).

The starting materials were made by mixing equal masses of natural magnesite with either synthetic $MgSiO_3$ glass or reagent grade $CaCO_3$ (>99.99% purity). Before weighing, the individual components were dried at 220°C for more than 24 hours. After a minimum of 30 minutes grinding under ethanol in an agate mortar, ~ 10 wt.% platinum black was added to each mix as a laser absorber. Subsequently,

mixes were ground for a further 2-3 hours to ensure homogeneity and to reduce the grainsize of the Pt black; particles are observed to be predominantly sub-micron, but with the occasional grain in the one to ten micron range that are avoided. In order to ensure that the systems remain iron-free the crucibles and agate mortars had never previously been used with iron-bearing compositions. EDS analysis revealed that the $MgCO_3$-$CaCO_3$ starting mix contains minor contamination of up to 0.5 wt% SiO_2 in the bulk.

2.1 Off-line LH-DAC experiments on $MgSiO_3$-$MgCO_3$ and $MgCO_3$-$CaCO_3$

Experiments were performed in Princeton-type symmetric DACs using anvils with standard 250μm culets (200μm culet diamonds were used in the highest pressure $MgCO_3$-$CaCO_3$ experiment). Rhenium was used as the gasket material, pre-indented to ~ 25 GPa. Three or four 30-40μm sized holes were drilled in the central portion of each gasket using an UV laser ablation unit (New Wave research, LUV series, operating wavelength 266 nm) creating multiple, physically separated sample chambers (see figure 1a). A single starting mix, either $MgSiO_3$-$MgCO_3$ or $MgCO_3$-$CaCO_3$, was loaded into all the sample chambers, to eliminate the possibility of cross-contamination. A single ruby grain (< 2-3μm) was added to one of the sample chambers. Each loaded cell was heated at 125°C for 1 hour prior to sealing in order to eliminate any adsorbed water contamination acquired during loading.

Pressure was monitored in one chamber during compression using the shift in the R1 ruby fluorescence peak as calibrated by Mao et al. (1986). Pressure was measured at room temperature after the experiment in all chambers using two different methods. Firstly, the ruby scale pressure was determined in the ruby-bearing chamber. Then, pressure in all sample chambers was measured using the shift of the 1332 cm^{-1} Raman peak of diamond at the culet surface measured with a custom-built

confocal Raman system. The Raman peak shift, Δν, was converted to sample chamber pressure using a calibration curve specific to the materials used as pressure media (e.g. the sample mixes). The calibration was made by plotting the ruby pressure vs. Δν for the ruby-bearing chambers in all experiments, as shown in Fig. 2. A highly correlated linear relation exists between ruby pressure and Δν, with a measurement precision in each reported pressure of ± 1.9 GPa at one standard error; pressure accuracy is tied to the ruby scale. This method of pressure measurement is preferred as it avoids possible contamination with ruby (Al_2O_3) during laser heating, and allows pressure to be measured directly adjacent to the heated region thereby minimising the effects of pressure gradients. Reported pressures are those recorded post-heating. Thermal pressure during heating was estimated in one experiment as described below.

Samples were laser heated in a double-sided configuration using a pair of 100 W diode-pumped fibre lasers (TEM_{00}) emitting at 1070 nm. The Gaussian energy distribution of the lasers can generate strong temperature gradients in the sample. Such gradients are undesirable as they exacerbate errors in temperature measurement related to chromatic aberration (Walter and Koga, 2004), can lead to Soret diffusion, and increase the sensitivity of measured temperature to system alignment. Therefore, we have employed beam shaping optics combined with variable beam expanders to create a flat-topped energy profile at the sample surface of up to ~30 μm diameter. This setup can yield a nearly isothermal temperature at the surface of uniformly absorbing samples. In the experiments reported here, the temperature distribution across the sample is observed to depend considerably on the distribution of the Pt absorber within the flat-topped energy profile. Laser power was increased automatically (after an initial temperature of 1600-1700 K was reached) in linear steps with intervals of 7 seconds with a temperature measured at each interval. Experiments lasted 3-10 minutes in total duration.

Temperature was measured along a vertical profile located centrally across the heated region on both sides of the sample simultaneously, using standard imaging spectroradiometry techniques. Details of the optical configuration, procedures and calibrations are presented in full elsewhere (Lord *et al.,* submitted; 2010; 2009; Walter and Koga, 2004), but a brief description of salient points is presented here. We focus the lasers and image the sample using a 20 mm focal length Mitotoyu apochromatic lens designed for radiation in the near-infrared. The light from the sample is focused at the spectrometer slit (image plane) using a 1 metre f achromatic doublet, which in combination with the objective yields a magnification of 50x. On the basis of the magnification and detector pixel size, our system has an ideal resolution of ~ 0.5 μm. However, the diffraction limit at 700 nm, which is the nominal central wavelength used in the spectral fitting, is ~ 1.3 μm, defining the maximum spatial resolution that can practically be achieved. Optical aberrations can further reduce the resolution. Based on measurements using a resolution target the diffraction limit is achieved in our system for a flat-field illumination. However, chromatic aberrations can further limit the effective spectroradiometric resolution if a temperature gradient is present (Boehler and Chopelas, 1991; Walter and Koga, 2004; Benedetti *et al.,* 2009). On the basis of the measured focal deviations of our system (maximum of ± 5 μm at the image plane over the 200 nm spectral window), we calculate a worst-case spectroradiometric resolution of ~ 3 μm at the sample surface (object plane). Errors associated with chromatic aberration can be deduced from the precision of the spectral fits to the ideal greybody Wien function, and are a function of the temperature gradient (Walter and Koga, 2004). The precision of the spectral fits reported here are typically less than 5 K, and in all cases < 10 K, indicating that chromatic effects are not a significant component of the fits. All things considered, we make a conservative estimate of error in calculated temperatures associated with optical aberrations of less than 50 K, and likely less than 25

K. The accuracy of the temperature measurement system has previously been tested at ambient pressure against the known melting points of a range of metals (Lord *et al.,* 2009; 2010) and is estimated at 50-200 K. The source of this inaccuracy is likely the unknown emissivity of the samples used in calibration, a parameter that is both material specific and dependent on temperature and pressure. Because we have very little information regarding the emissivity of our samples, we choose not to include this error in our reported uncertainties, but simply acknowledge that it exists. It is also noteworthy that where our data overlap with those of previous multi-anvil experiments we find a very good consistency in melting temperature (see below).

2.2 In-situ LH-DAC experiment on $MgCO_3$-$CaCO_3$

Unlike the off-line experiments (§2.1), this experiment employed a single, 100μm diameter sample chamber. The sample chamber was filled with a foil of sample material containing platinum black sandwiched between foils of the same composition without platinum black, which act as both pressure medium and thermal insulation. The foils were created by compressing powder between diamond anvils and pieces of appropriate size were chosen for loading. A single ruby grain was placed on the edge of the sample chamber to allow the pressure to be monitored during compression. Laser heating was performed using a double-sided, off-axis geometry generating a heated spot of ~ 30 μm diameter. The incandescent light is collected using reflective optics and a 2 x 2 μm region at the centre of the heated spot is selected for temperature measurement. Temperatures on both sides are equalised before the experiment, but only measured on the upstream side during the experiment to allow simultaneous XRD. For further details see Schultz *et al.* (2005). The 33 keV X-ray beam (λ = 0.3738 Å) had a FWHM of 4 μm and was aligned with the centre of the heated spot using the X-ray induced fluorescence of the sample. Diffraction patterns were collected on a MAR345 CCD using an exposure

time of 15 seconds. The distance between sample and detector was calibrated using a LaB_6 standard. X-ray diffraction patterns were taken before, periodically throughout and after sample heating. 2-D XRD patterns were masked and integrated into 1-D patterns using Fit2D (Hammersley, 1997). These patterns were in turn fitted and analysed using the Le Bail method (Le Bail *et al.*, 1988) as implemented in the GSAS suite of programmes (Larson and Von Dreele, 2000; Toby, 2001). The pressure in this experiment was calculated from the measured unit cell volume of the platinum laser absorber and the measured temperature using the Mie-Grüneisen-Debye P-V-T equation of state (EOS) for platinum of Zha *et al.* (2008).

2.3 Melt Detection

We use multiple criteria to deduce the temperature at which the sample melts during laser heating, of which the primary criterion is a discontinuity in the temperature vs. laser power curve generated during the heating ramp. The key perturbation is the development of a temperature plateau, where over some range of increasing power, temperature remains essentially constant or oscillates around some value. Temperature plateaux have been used extensively as a melting criterion in the LH-DAC (e.g. Lord *et al.,* 2009; 2010; submitted; Fischer et al., 2013; Asanuma et al., 2010), and are well correlated with independent observations of melting using in situ X-ray diffraction techniques (Fischer et al., 2013; Lord *et al.,* submitted). The exact causes of the perturbations are difficult to assess fully, but are likely related to a combination of differences in the thermal properties of the co-existing solid and liquid phases during melting and changes in sample absorption properties (Lord *et al.,* submitted; 2010; Geballe and Jeanloz, 2012). In the experiments reported here where an extrinsic absorber (Pt black) is used, mechanical changes in the sample upon melting and subsequent redistribution of the Pt grains also contributes to the perturbation, and can be recognized by variations in the shape of the temperature

profile that occur once a plateau is reached. Finally, using a variable neutral density filter and a CCD camera we can visually observe movement in the sample (mechanical or convective) that occurs once the temperature plateau is reached. After melting begins, during the temperature plateau, we observe that the Pt absorbers often migrate away from the melted-region and often form a bright doughnut shape that expands as the experiment continues.

In experiments on the $MgSiO_3$-$MgCO_3$ system the discontinuities that define melting are flat plateaux and are also extremely stable, remaining at constant temperature until the end of the experiment (figure 3). In this case the melting temperature is defined as the average of all temperatures within the plateau. The uncertainty associated with the melting temperature is reported as twice the standard deviation of all the temperature measurements in the plateau (2σ).

$MgCO_3$-$CaCO_3$ experiments display a slightly different behaviour. Discontinuities in this system do not typically appear as long, stable plateaux, but instead as a short plateau followed by rising temperatures (figure 4). On close inspection of individual temperature profiles collected throughout the heating ramp it can be seen that increasing temperatures after the short plateau are caused by the presence of localised hotspots of platinum-rich material at temperatures above the liquidus of the sample. As this superheating continues, often the entire sample becomes heated to super-liquidus temperatures, during which time convection is observed to be vigorous. During the subsolidus heating ramp, samples can display considerable temperature topographies depending on the initial distribution of platinum within the sample chamber (Fig. 1). When the melting temperature is reached the temperature profile across the sample becomes flatter as convection begins to occur. Once the temperature across the entire sample has equalised, the platinum-rich hotspots begin to form. A schematic illustration of this process

can be seen in figure 1b and an example of real data can be seen in figure 1c. Due to the presence of this behaviour the definition of the melting temperature in $MgCO_3$-$CaCO_3$ experiments is based on a combination of three criteria, not all of which are always observed in each experiment. These are a) the observation of a limited plateau, b) visible convective motion of the sample and c) the loss of any subsolidus topography in temperature profiles as the melting temperature is reached. It is also worth noting that in all cases a break in slope of the temperature-power curve is seen at the point of initial melt generation (see figures 3 and 4) and that all three criteria provide the same result. As the plateaux in this system are much shorter the uncertainty in the melting temperature has often been conservatively estimated, instead of reporting a standard deviation value based on fewer than 10 data points.

In some experiments there was a significant difference between temperatures measured on each side of the DAC throughout heating. As chromatic aberration is insignificant (see above) it is suggested that this is caused either by poor laser coupling or by misalignment of the emitted light with the spectrometer entrance slit on one side of the system. This is likely due to the difficulties in perfectly aligning the system at low temperatures, when the emitted light is weak. When this occurs only the higher temperature side is used to determine melting temperatures (e.g. fig 3c), as misalignment will cause an underestimation, and never an overestimation, of true temperature.

2.4 Ex-situ Sample Analysis

After complete pressure release samples were recovered from the DAC and selected $MgSiO_3$-$MgCO_3$ experiments mounted in epoxy to permit *ex-situ* analysis. Samples were polished by hand using 0.3 μm alumina-impregnated Mylar sheets prior to Ar-ion polishing using a Technoorg Linda ion mill.

277 Textural and chemical analyses were performed using the JEOL JXA8530F Field Emission Gun
278 Electron Microprobe at the University of Bristol operated at 5-9 keV and 20 nA over three analytical
279 sessions. The system was calibrated using St John's Island olivine and platinum metal as primary
280 standards and was verified with diopside as a secondary standard.
281
282 **3. RESULTS**
283 *3.1 Enstatite-Magnesite*
284 All melting experiments in the enstatite-magnesite system produced clearly defined plateaux in
285 temperature vs. laser power that were used to define the eutectic melting temperature (figure 3).
286 Previous work (Newton *et al.,* 1975; Katsura and Ito, 1990; Koziol and Newton, 1998) has shown that
287 this system becomes a simple binary above ~5 GPa and up to 15 GPa, producing a eutectic melt at
288 2073 - 2173 K at 15 GPa. As there are no known phases with intermediate compositions we assume
289 that the system continues to behave similarly throughout all the high pressures experiments of this
290 study. The measured eutectic temperatures and associated errors are listed in Table 1 and plotted as a
291 function of pressure in figure 5a.
292
293 The lowest pressure experiment in this study was conducted at 16 ± 2 GPa and was found to melt at
294 2080 ± 40 K. This is within the temperature bracket for eutectic melting of previous experiments
295 determined from *ex-situ* analysis of multi-anvil press experiments (Katsura and Ito, 1990), providing
296 further credibility for the accuracy of both our temperature measurement and melting criteria. With
297 increasing pressure the eutectic temperatures decrease, reaching a minimum at ~ 23 GPa. It is clearly
298 not possible to fit a single melting curve to the entire dataset, as there is a change in melting slope at ~
299 23 GPa. This pressure corresponds to the location of the phase change from ilmenite- to perovskite-

This is a preprint, the final version is subject to change, of the American Mineralogist (MSA)
Cite as Authors (Year) Title. American Mineralogist, in press.
(DOI will not work until issue is live.) DOI: http://dx.doi.org/10.2138/am.2014.4735

300 structured $MgSiO_3$ (Ono *et al.,* 2001) at the solidus. The melting curve in the interval 5 – 23 GPa marks
301 the reaction ilmenite $MgSiO_3$ + magnesite = melt and is defined by a polynomial with coefficients
302 reported in table 2; all data collected at pressure < 24.5 GPa are used in this fit.
303
304 At pressures above ~ 23 GPa, the eutectic temperature rises consistently to 2350 ± 75 K (2σ) at 80 GPa.
305 The experiments above 22 GPa were fitted using a damped Simon-Glatzel melting equation
306 ($T_m = T_t\left(\frac{P}{a}+1\right)^{\frac{1}{b}}\exp(-cP)$), Simon and Glatzel, 1929; Kechin, 2002) with coefficients reported in
307 table 2. This defines the eutectic melting curve where the reaction perovskite $MgSiO_3$ + magnesite =
308 melt. The intersection of the two fitted curves at ~ 23 GPa represents the triple point corresponding to
309 the assemblage magnesite + ilmenite + perovskite + liquid. Figure 5a shows that this point falls almost
310 exactly upon the ilmenite + perovskite phase boundary in the $MgSiO_3$ system previously determined
311 using *in-situ* experiments (Ono *et al.,* 2001). With increasing pressure dT/dP decreases such that the
312 estimated melting temperature at the core mantle boundary (135 GPa), assuming no further phase
313 changes occur, is 2522 ± 131 K (2σ).
314
315 *Ex-situ* analysis of subsolidus runs performed at ~ 100 and 300 K below the melting point at ~ 35 GPa
316 (T_m^{35} = 2104 ± 69 K) reveal experimental products consisting only of coexisting crystals of perovskite
317 and magnesite approximately 1 - 3μm in size (figure 6a). Crystal compositions were confirmed as
318 stoichiometric $MgSiO_3$ and $MgCO_3$ (CO_2 by difference) using multiple quantitative analyses and WDS
319 element maps. In these experiments the platinum laser absorber remains evenly distributed as small (<
320 1μm) grains throughout the sample chamber. A third experiment in the same gasket (31.5 GPa, T_{max} =
321 2040 K) was quenched within 15 seconds of achieving the melting temperature. This experiment also
322 has a larger grain size (up to ~ 10 μm) in one portion of the experiment, assumed to correspond to the

location of heating. No phases other than perovskite, magnesite or Pt metal were observed in this experiment.

The textural and chemical features observed in the recovered experiments that were interpreted as having partially melted (using the plateau and other criteria described above) are significantly different than the subsolidus runs. The location of the centre of the heated spot is clearly defined either by the small grain size in the central region due to quench crystallisation or the annular distribution of phases in the experiments (e.g. figure 6b and c). We observe that phase separation occurred in the molten region, with grains of MgO, SiO_2 and diamond identified. It is also observed that the platinum absorber has migrated away from the centre of this region and often formed clumps at the boundary with surrounding material (figure 6c). Outside this central area the samples consist of $MgSiO_3$ and $MgCO_3$ with well-dispersed Pt, as seen in subsolidus runs. Within the hotspot region MgO grains are most commonly found in areas near the sample surfaces, adjacent to the diamond culets (figure 6b), whilst SiO_2 is only observed in the central region of the sample (figure 6c). This axial phase distribution was confirmed by analysing the same experiments at two different levels during subsequent analysis sessions (e.g. figure 6b and c) and has been confirmed in experiments conducted at ~ 18, 27 and 36 GPa. The phase distribution corresponds to SiO_2 migration towards the hotter regions and MgO migration towards the cooler regions of the sample, a feature that results from Soret diffusion in LH-DAC experiments (Sinmyo and Hirose, 2010). The changes observed in the textural and chemical features between subsolidus and molten conditions provide further confirmation that our *in-situ* criteria are reliable indicators of melting. However, the estimation of melt compositions is prevented by phase separation occurring after melting and is beyond the scope of this study.

346 *3.2 Magnesite-Calcite*

347 Previously, the minimum melting point in the $MgCO_3$-$CaCO_3$ system had been defined at 1, 2.7 and 6
348 GPa (Byrnes and Wyllie, 1981; Irving and Wyllie, 1975; Buob *et al.*, 2006 respectively), corresponding
349 to the reaction dolomite$_{ss}$ = melt. Our experimental data points range from 16 – 80 GPa (table 1 and
350 figure 5b) and corresponds to the reaction magnesite + aragonite = melt (confirmed by *in-situ*
351 experiment and the previous study of Luth, 2001). We observe that the melting temperature increases
352 as pressure rises to above ~ 35 GPa, above which the melting temperature is nearly constant at ~ 2100
353 K and possibly decreases with continued pressure increase. The fitting coefficients corresponding to the
354 parameterised melting curve in figure 5b and 7 are presented in table 2. The melting temperature at 135
355 GPa, again assuming no phase changes occur in the intervening pressure interval, is 1994 ± 239 K (2σ).
356
357 The single *in situ* experiment undertaken at ESRF was used to confirm that the melting temperatures
358 determined from the off-line experiments do indeed represent a eutectic melting reaction, rather than a
359 subsolidus phase change. The post-heating pressure of the experiment, calculated from the room
360 temperature EoS of platinum (Zha *et al.*, 2008), was 45.7 GPa. The pressure during melting (2030 K)
361 was 52.4 GPa, implying a thermal pressure of 6.7 GPa (~15%). This experiment avoided the effect of
362 hotspot growth as temperature was only measured in a single spot aligned with the x-ray beam within
363 the centre of the melt pool. The maximum temperature reached in this experiment was 2066 K and the
364 melting temperature is estimated as 1990 ± 90 K from a clearly defined plateau. Dynamic
365 recrystallisation, indicated by the appearance of saturated spots that move between consecutive
366 diffraction patterns, was observed throughout the temperature plateau. The melting temperature is
367 slightly lower than (but within error of) the melting curve defined by the off-line experiments. The
368 same three-component phase assemblage was present before, during (figure 7) and after heating:

magnesite, post-aragonite structured $CaCO_3$ (Ono *et al.,* 2005) and platinum. There is one peak that cannot be fitted at a d-spacing of ~ 2.65Å that was present before, during and after the experiment, so is not thought to be involved in a reaction. It does not match the position of any expected peaks from materials that might be expected to be present, such as Re, Al_2O_3, MgO or diamond. This experiment confirms that there is no chemical reaction or subsolidus phase change occurring, but rather, plateaux correspond to the eutectic melting of $MgCO_3$-$CaCO_3$ at lower mantle pressures.

3.3 Effect of thermal pressure

In our study we have reported all pressures as post-heating pressures, without any correction for the possible effect of thermal pressure. The thermal pressure was determined in the single *in-situ* experiment as ~ 15% of the post-heating pressure. However, as the sample geometry employed during the *in-situ* experiment was significantly different from that during all off-line experiments there is no reason to believe this thermal pressure should apply to all experiments. Furthermore, the proximity of the known ilmenite/perovskite phase boundary and the pressure at which we observe the cusp in the $MgSiO_3$-$MgCO_3$ melting curve suggests that thermal pressure is negligible.

4. DISCUSSION

The occurrence of carbonated melting in the deep mantle depends on whether carbonates are stable at high pressure. As suggested in the introduction, there is significant uncertainty about whether carbon is present in oxidized or reduced forms throughout the mantle. The oxygen fugacity required to reduce carbonate to diamond is thought to be 2-3 orders of magnitude above the iron-wüstite buffer (Stagno *et al.,* 2011), and would be reached for ferric/ferrous ratios typical of the lithospheric mantle at depths in excess of ~ 200 km. The extent to which lithospheric mantle is representative of the ambient mantle is

unclear, but it suggests that melting curves of carbonated lithologies might only be applicable to abnormally oxidised regions of the mantle where carbonates remain stable.

If we assume that redox conditions allow carbonate stability then the system $MgSiO_3$-$MgCO_3$ is a proxy for the behaviour of carbonated silica-poor mantle material, i.e. the peridotitic mantle or lowermost portions of subducting assemblages. The results of this study imply that a model magnesite + enstatite/perovskite mantle would be subsolidus along a mantle adiabat (e.g. Katsura, 2010) in the upper mantle and transition zone. However, due to the cusp along the solidus associated with the ilmenite-perovskite transition, this model carbonated mantle would begin melting at pressures in excess of ~ 35 GPa (figure 8). The addition of other chemical components, especially alkalis, would be expected to reduce the solidus and smear out the cusp, but a solidus depression, even a deep one, might still be expected in a natural carbonated peridotite system; previous experimental data are consistent with this interpretation. Ghosh *et al.* (2009) bracketed the solidus of carbonated peridotite from 10-20 GPa using multi-anvil experiments, and data from their study are plotted in figure 9 alongside the melting curves of carbonated peridotite from natural and model systems. Ghosh *et al.* (2009) suggest a flat melting curve above ~ 14 GPa, but a negative $\partial P/\partial T$ slope from 16 – 20 GPa as indicated by our data in the simple MgO-SiO_2-CO_2 system is also consistent with their experimental data. Ghosh *et al.* (2009) suggested that the close relationship of the mantle geotherm with the carbonated peridotite solidus could lead to a region of melting at the top of the lower mantle. Our new data showing a cusp along the solidus related to the subsolidus transition to a perovskite-bearing lower mantle strengthens this interpretation considerably, and indicates that the upper/lower mantle boundary could be a potential location where carbonate melts are produced.

Slab materials undergo hydrous melting at sub-arc pressures, causing loss of alkali and water components (Yaxley and Green, 1994; Molina and Poli, 2000; Kerrick and Connolly, 2001; Connolly, 2005; Poli *et al.*, 2009), but are thought to retain the majority of their carbon. It is also likely that redox conditions in the remnants of subducted materials are more oxidising than the ambient mantle, and thus carbonates are the dominant carbon species. In this situation the system $MgCO_3$-$CaCO_3$ is an appropriate proxy for carbonate-rich components of subducting assemblages whereas the $MgSiO_3$-$MgCO_3$ system is relevant to peridotitic (or SiO_2 undersaturated) portions. Based on subduction geotherms from Syracuse *et al.* (2010) and the shallow or flat solidi defined in this study, it is expected that these portions of subducted assemblages will experience melting within the lower mantle (figure 8). It is uncertain whether carbonated eclogite material will experience a similar fate as the study of Seto *et al.* (2008) suggests that silica-rich compositions experience a different behaviour at lower mantle pressures.

Carbonate melts have been shown to be highly mobile in the upper mantle (Hammouda and Laporte, 2000) and would be expected to rapidly percolate into surrounding mantle regions. Upon reaching a reduced mantle domain (normal ambient mantle) it has been experimentally shown that they will undergo 'redox-freezing' reactions to form diamond and other minerals (Rohrbach and Schmidt, 2011). As this study suggests that carbonated melting occurs in the upper/lower mantle boundary region it is also implied that a significant amount of diamond formation might occur in this region, provided that carbonate melts remain mobile at these pressures. Diamonds from the transition zone and lower mantle that have been discovered worldwide may share a common origin related to melting of carbonated protoliths and redox driven crystallization (see Harte, 2010 for a review of sub-lithospheric diamonds).

5. IMPLICATIONS

Our study implies that, if conditions are sufficiently oxidising, carbonate phases will melt along a geotherm throughout the lower mantle. The Clausius-Clapeyron slope of both melting curves indicate that low-degree melting of subducted carbonated lithologies is expected to be widespread at lower mantle depths. Extrapolation of our melting curves suggest that the maximum temperature of carbonate stability in the mantle is ~ 2500 K. The initiation of carbonated melting near the upper/lower mantle boundary that is predicted by our data can help explain the widespread discovery of 'superdeep' diamonds from this depth interval.

A further possible consequence of our results relates to the observation that the slopes of both melting curves presented (dT/dP) approach zero, or become negative, at high pressures. Given the relationship $dT/dP = \Delta V/\Delta S$ it is implied, assuming that ΔS is positive for the melting reaction, that the density of the melt approaches, or possibly becomes greater than that of the residual solid with increasing pressure. Therefore, if any carbonated material does survive to lower mantle depths the melts they eventually produce may be neutrally, or even negatively, buoyant allowing them to become trapped in the lower mantle. This would allow the creation of a carbon-rich reservoir hidden from materials sampled at the Earth's surface. This hidden reservoir could balance the superchondritic H/C composition of the bulk Earth (Hirschmann and Dasgupta, 2009), thus removing the reliance on either carbon storage in the core, removal of a CO_2 atmosphere or a non-chondritic late-veneer to explain the bulk earth's volatile budget.

6. ACKNOWLEDGEMENTS

This work was supported by the Natural Environmental Research Council by grants awarded to ART at Bristol (grant number NE/J500033/1), MJW at Bristol (grant number NE/I010947/1) and Lidunka Volčado at UCL (grant number NE/H003975/1). We would like to thank Craig Manning and an anonymous reviewer for their constructive feedback and Daniel Hummer for his editorial handling of this paper. We acknowledge the European Synchrotron Radiation Facility for provision of synchrotron radiation facilities and we would like to thank Mohamed Mezouar for assistance in using beamline ID27.

7. REFERENCES

Asanuma, H., Ohtani, E., Sakai, T., Terasaki, H., Kamada, S., Kondo, T., and Kikegawa, T. (2010) Melting of iron–silicon alloy up to the core–mantle boundary pressure: implications to the thermal structure of the Earth's core. Physics and Chemistry of Minerals, 37, 353-359.

Benedetti, L.R., Farber, D.L., and Kavner, A. (2009) The great wedge: Quantifying chromatic aberration in imaging spectroscopy systems and application to temperature measurements in the laser-heated diamond anvil cell. Journal of Applied Physics, 105 (2), 023517.

Berg, G.W. (1986) Evidence for carbonate in the mantle. Geology, 324, 50-51.

Boates B., Teweldeberhana, A.M., and Boneva, S.A. (2012) Stability of dense liquid carbon dioxide. Proceedings of the National Academy of Sciences, 109 (37), 14808-14812.

Boehler, R., and Chopelas, A. (1991) A New approach to laser-heating in high-pressure mineral physics. Geophysical Research Letters, 18 (6), 1147-1150.

Buob, A., Luth, R.W., Schmidt, M.W., and Ulmer, P. (2006) Experiments on $CaCO_3$-$MgCO_3$ solid solutions at high pressure and temperature. American Mineralogist, 91, 435-440.

Byrnes, A.P. and Wyllie, P.J. (1981) Subsolidus and melting relations for the join $CaCO_3$-$MgCO_3$ at 10-kbar. Geochimica et Cosmochimica Acta, 45, 321-328.

Connolly, J.A.D. (2005) Computation of phase equilibria by linear programming: A tool for geodynamic modelling and its application to subduction zone decarbonation. Earth and Planetary Science Letters, 236, 524-541.

Dalton, J.A., and Presnall, D.C. (1998) Carbonatitic melts along the solidus of model lherzolite in the system CaO-MgO-Al2O3-SiO2-CO2 from 3 to 7 GPa. Contributions to Mineralogy and Petrology, 131, 123-135.

Dasgupta, R., Hirschmann, M.M., and Withers, A.C. (2004) Deep global cycling of carbon constrained by the solidus of anhydrous, carbonated eclogite under upper mantle conditions. Earth and Planetary Science Letters, 227, 73-85.

Dasgupta, R. (2013) Ingassing, storage, and outgassing of terrestrial carbon through geologic time. Reviews in Mineralogy and Geochemistry, 75, 183-229.

Dasgupta, R., and Walker D. (2008) Carbon solubility in core melts in a shallow magma ocean environment and distribution of carbon between the Earth's core and the mantle. Geochimica et Cosmochimica Acta, 72, 4627-4641.

Dasgupta, R., and Hirschmann, M.M. (2010) The deep carbon cycle and melting in Earth's interior. Earth and Planetary Science Letters, 298, 1-13.

Dasgupta, R., Mallik, A., Tsuno, K., Withers, A.C., Hirth, G., and Hirschmann, M.M. (2013) Carbon-dioxide-rich silicate melt in the Earth's upper mantle. Nature, 493, 211-215.

Fiebig, J., Chiodini, G., Caliro, S., Rizzo, A., Spangenberg, J., and Hunziker, J.C. (2004) Chemical and isotopic equilibrium between CO_2 and CH_4 in fumarolic gas dischrages: Generation of CH_4 in arc magmatic-hydrothermal systems. Geochimica et Cosmochimica Acta, 68, 2321-2334.

Fischer R.A., Campbell A.J., Reaman D.M., Miller N.A., Heinz D.L., Dera P., and Prakapenka V.B. (2013) Phase relations in the Fe–FeSi system at high pressures and temperatures. Earth and Planetary Science Letters, 373, 54-64

Franzolin, E., Schmidt, M.W., and Poli, S. (2011) Ternary Ca–Fe–Mg carbonates: subsolidus phase relations at 3.5 GPa and a thermodynamic solid solution model including order/disorder. Contributions to Mineralogy and Petrology, 161, 213-227.

Frezzotti, M.L. Selverstone, J., Sharp, Z.D., and Compagnoni, R. (2011) Carbonate dissolution during subduction revealed by diamond-bearing rocks from the Alps. Nature Geoscience, 4, 703-706.

Frost, D.J., and McCammon, C.A. (2008) The redox state of the Earth's mantle. Annual Review of Earth and Plametary Sciences, 36, 389-420.

Gaillard, F., Mohammed, M., Iacono-Marziano, G., Pichavant, M., and Scaillet, B. (2008) Carbonatite melts and electrical conductivity in the asthenosphere. Science, 322, 1363-1365.

Geballe, Z., and Jeanloz, R. (2012) Origin of temperature plateaus in laser-heated diamond anvil cell experiments. Journal of Applied Physics, 111, 123518, doi: 10.1063/1.4729905.

Ghosh, S., Ohtani, E., Litasov, K.D., and Terasaki, H. (2009) Solidus of carbonated peridotite from 10 to 20 GPa and origin of magnesiocarbonatite melt in the Earth's deep mantle. Chemical Geology, 262, 17-28.

Gorman, P.J., Kerrick, D.M., and Connolly, J.A.D. (2006) Modeling open system metamorphic decarbonation of subducting slabs. Geochemistry Geophysics Geosystems, 7, Q04007.

Hammersley, A.P. (1997) FIT2D: an introduction and overview, Technical Report ESRF-97-HA-02T, ESRF, Grenoble.

Hammouda, T., and Laporte, D. (2000) Ultrafast mantle impregnation by carbonatite melts. Geology, 28 (3), 283-285.

Hammouda, T. (2003) High-pressure melting of carbonated eclogite and experimental constraints on carbon recycling and storage in the mantle. Earth and Planetary Science Letters, 214, 357-368.

Harte, B., (2010) Diamond formation in the deep mantle: the record of mineral inclusions and their distribution in relation to mantle dehydration zones. Mineralogical Magazine, 74(2), 189-215.

Irving, A.J., and Wyllie, P.J. (1975) Subsolidus and melting relationships for calcite, magnesite and join $CaCO_3$-$MgCO_3$ to 36 Kbar. Geochimica et Cosmochimica Acta, 39, 35-53.

Isshiki, M., Irifune, T., Hirose, K., Ono, S., Ohishi, Y., Watanuki, T., Nishibori, E., Takata, M., and Sakata, M. (2004) Stability of magnesite and its high-pressure form in the lowermost mantle. Nature, 427, 60-63.

Katsura, T., and Ito, E. (1990) Melting and subsolidus phase relations in the $MgSiO_3$-$MgCO_3$ system at high pressures: implications to evolution of Earth's atmosphere. Earth and Planetary Science Letters, 99, 110-117.

Katsura, T., Yoneda, A., Yamazaki, D., Yoshino, T., and Ito, E. (2010) Adiabatic temperature profile in the mantle. Physics of Earth and Planetary Interiors, 183, 212-218.

573 Kechin, V.V. (2002) Melting curve equations at high pressure. Physical Review B, 65(5), doi:
574 10.1103/PhysRevB.65.052102
575
576 Kerrick, D.M., and Connolly, J.A.D. (2001) Metamorphic devolatilization of subducted marine
577 sediments and the transport of volatiles into the Earth's mantle. Nature, 411, 293-296.
578
579 Keshav, S., and Gudfinnsson, G.H. (2010) Experimentally dictated stability of carbonated oceanic crust
580 to moderately great depths in the Earth: Results from the solidus determination in the system CaO–
581 MgO–Al_2O_3–SiO_2–CO_2. Journal of Geophysical Research - Solid Earth, 115. doi:
582 10.1029/2009JB006457.
583
584 Kiseeva, E.S., Yaxley, G.M., Hermann, J., Litasov, K.D., Rosenthal, A., and Kamenetsky, V.S. (2012)
585 An experimental study of carbonated eclogite at 3·5–5·5 GPa - implications for silicate and carbonate
586 metasomatism in the cratonic mantle. Journal of Petrology 53, 727-759.
587
588 Kiseeva, E.S., Litasov, K.D., Yaxley, G.M., Ohtani, E., and Kamenetsky, V.S. (2013) Melting and
589 Phase Relations of Carbonated Eclogite at 9–21 GPa and the Petrogenesis of Alkali-Rich Melts in the
590 Deep Mantle. Journal of Petrology, 54, 1555-1583
591
592 Koziol, A.M., and Newton, R.C. (1998) Experimental determination of the reaction: Magnesite +
593 enstatite = forsterite + CO_2 in the ranges 6-25kbar and 700-1100 degrees C. American Mineralogist,
594 83, 213-219.
595

596 Larson, A. C., and Von Dreele, R.B. (1994) General Structure Analysis System (GSAS), Los Alamos
597 National Laboratory Report LAUR 86-748.
598
599 Le Bail, A., Duroy, H., and Fourquet, J.L. (1988) *Ab-initio* structure determination of $LiSbWO_6$ by X-
600 ray powder diffraction. Materials Research Bulletin 23, 447-452.
601
602 Litasov, K.D., Fei, Y., Ohtani, E., Kuribayashi, T., and Funakoshi, K., (2008) Thermal equation of state
603 of magnesite to 32 GPa and 2073 K. Physics of the Earth and Planetary Interiors, 168, 191-203.
604
605 Litasov, K., and Ohtani, E. (2010) The solidus of carbonated eclogite in the system $CaO–Al_2O_3–MgO–$
606 $SiO_2–Na_2O–CO_2$ to 32 GPa and carbonatite liquid in the deep mantle. Earth and Planetary Science
607 Letters, 295, 115-126.
608
609 Litasov, K.D., Goncharov, A.F., and Hemley, R.J. (2011) Crossover from melting to dissociation of
610 CO2 under pressure: Implications for the lower mantle. Earth and Planetary Science Letters, 309, 318-
611 323.
612
613 Lord, O.T., Walter, M.J., Dasgupta, R., Walker, D., and Clark, S.M. (2009) Melting in the Fe-C system
614 to 70 GPa. Earth and Planetary Science Letters, 284, 157-167.
615
616 Lord, O.T., Walter, M.J., Dobson, D.P., Armstrong, L., Clark, S.M., and Kleppe, A. (2010) The FeSi
617 phase diagram to 150 GPa. Journal of Geophysical Research, 115, B06208.
618

Lord, O.T., Wann, E.T.H., Hunt, S.A., Walker, A.M., Santangelli, J., Walter, M.J., Dobson, D.P., Wood, I.G., Vocadlo, L, Morard, G., and Mezouar, M. (submitted) The NiSi melting curve to 70 GPa. Physics of the Earth and PIanetary Interiors.

Luth, R.W. (1993) Diamonds, eclogites, and the oxidation state of the Earth's mantle. Science, 261, 66-68.

Mao, H.K., Xu, J., and Bell, P.M. (1986) Calibration of the ruby pressure gauge to 800-kbar under quasi-hydrostatic conditions. Journal of Geophysical Research – Solid Earth and Planets, 91, 4673-4676.

Martin, A.M., Laporte, D., Koga, K.T., Kawamoto, T., and Hammouda, T. (2012) Experimental Study of the Stability of a Dolomite + Coesite Assemblage in Contact with Peridotite: Implications for Sediment – Mantle Interaction and Diamond Formation During Subduction. Journal of Petrology, 53, 391-417.

McCammon, C., Hutchison, M., and Harris, J. (1997) Ferric iron content of mineral inclusions in diamonds from Sao Luiz: A view into the lower mantle. Science, 278, 434-436.

Molina, J.F., and Poli, S. (2000) Carbonate stability and fluid composition in subducted oceanic crust: an experimental study on H_2O–CO_2–bearing basalts. Earth and Planetary Science Letters, 176, 295–310.

Newton, R.C., and Sharp, W.E. (1975) Stability of forsterite + CO_2 and its bearing on role of CO_2 in mantle. Earth and Planetary Science Letters, 26, 239-244.

Ono, S., Katsura, T., Ito, E., Kanzaki, M., Yoneda, A., Walter, M.J., Urakawa, S., Utsumi, W., and Funakoshi, K. (2001) *In situ* observation of ilmenite-perovskite phase transition in $MgSiO_3$ using synchrotron radiation. Geophysical Research Letters, 28, 835-838.

Ono, S., Kikegawa, T., Ohishi, Y., and Tsuchiya, J. (2005) Post-aragonite phase transformation in $CaCO_3$ at 40 GPa. American Mineralogist, 90, 667-671.

Oppenheimer, C., and Kyle, P.R. (2008) Probing the magma plumbing of Erebus volcano, Antartica, by open-path FTIR spectroscopy of gas emissions. Journal of Volanology and Geothermal Research, 177, 743-754.

Poli, S., Franzolin, E., Fumagalli, P., and Crottini, A. (2009) The transport of carbon and hydrogen in subducted oceanic crust: An experimental study to 5 GPa. Earth and Planetary Science Letters, 278, 350-360.

Rohrbach, A., and Schmidt, M. (2011) Redox freezing and melting in the Earth's deep mantle resulting from carbon–iron redox coupling. Nature, 472, 209-212.

Schultz, E., Mezouar, M., Crichton, W., Bauchau, S., Blattmann, G., Andrault, D., Fiquet, G., Boehler, R., Rambert, N., Sitaud, B., and Loubeyre, P. (2005) Double-sided laser heating system for in situ high

pressure-high temperature monochromatic X-ray diffraction at the ESRF. High Pressure Research, 25, 71-83.

Scott, H.P., Doczy, V.M., Frank, M.R., Hasan, M., Lin, J.F., and Yang, J. (2013) Magnesite formation from MgO and CO_2 at pressures and temperatures of the Earth's mantle. American Mineralogist, 98, 1211-1218.

Seto, Y., Hamane, D., Nagai, T., and Fujino, K. (2008) Fate of carbonates within oceanic plates subducted to the lower mantle, and a possible mechanism of diamond formation. Physics and Chemistry of Minerals, 35, 223-229.

Shilobreeva, S., Martinez, I., Busigny, V., Agrinier, P., and Laverne, C. (2011) Insights into C and H storage in the altered oceanic crust: Results from ODP/IODP Hole 1256D. Geochimica et Cosmochimica Acta, 75, 2237-2255.

Shirey, S.B., Cartigny, P., Frost, D.J., Keshav, S., Nestola, F., Nimis, P., Pearson, D.G., Sobolev, N.V., and Walter, M.J. (2013) Diamonds and the geology of mantle carbon. Reviews in Mineralogy and Geochemistry, 75, 355-421.

Simon F.E., and Glatzel G.Z., (1929) Remarks on fusion pressure curve. Zeitschrift fur Anorganische und Allgemeine Chemie, 178, 309-312.

687 Sinmyo, R., and Hirose, K., (2010) The Soret diffusion in laser-heated diamond-anvil cell. Physics of
688 the Earth and Planetary Interiors, 180, 172-178.
689
690 Sleep, N.H., and Zhanle, K. (2001) Carbon dioxide cycling and implications for climate on ancient
691 Earth. Journal of Geophysical Research 106, 1373–1399.
692
693 Stagno, V., and Frost, D.J. (2010) Carbon speciation in the asthenosphere: Experimental measurements
694 of the redox conditions at which carbonate-bearing melts coexist with graphite or diamond in peridotite
695 assemblages. Earth and Planetary Science Letters, 300, 72-84.
696
697 Stagno, V., Tange, Y., Miyajima, N., McCammon, C.A., Irifune, T., and Frost, D.J. (2011) The
698 stability of magnesite in the transition zone and the lower mantle as function of oxygen fugacity.
699 Geophysical Research Letters, 38, L19309.
700
701 Steinberger, B., and Torsvik, T.H. (2012) A geodynamic model of plumes from the margins of Large
702 Low Shear Velocity Provinces. Geochemistry Geophysics Geosystems, 13, Q01W09.
703
704 Syracuse, E.M., van Keken, P.E., and Abers, G.A. (2010) The global range of subduction zone thermal
705 models. Physics of The Earth and Planetary Interiors, 183, 73-90.
706
707 Teweldeberhan, A.M., Boates, B., and Bonev, S.A. (2013) CO_2 in the mantle: Melting and solid–solid
708 phase boundaries. Earth and Planetary Science Letters, 373, 228-232.
709

710 Toby, B.H. (2001) EXPGUI, a graphical user interface for GSAS. Journal of Applied Crystallography,
711 34, 210-213.
712
713 van der Meer, D.G., Spakman, W., van Hinsbergen, D.J.J., Amaru, M.L., and Torsvik, T.H. (2010)
714 Towards absolute plate motions constrained by lower-mantle slab remnants. Nature Geoscience, 3, 36-
715 40.
716
717 Walter, M.J., and Koga, K.T. (2004) The effects of chromatic dispersion on temperature measurement
718 in the laser-heated diamond anvil cell. Physics of the Earth and Planetary Interiors, 143, 541-588.
719
720 Walter, M.J., Kohn, S.C., Araujo, D., Bulanova, G.P., Smith, C.B., Gaillou, E., Wang, J., Steele, A.,
721 and Shirey, S.B. (2011) Deep Mantle Cycling of Oceanic Crust: Evidence from Diamonds and their
722 Mineral Inclusions. Science, 334, 54-57.
723
724 Woodland, A.B., and Koch, M. (2003) Variation in oxygen fugacity with depth in the upper mantle
725 beneath the Kaapvaal craton, Southern Africa. Earth and Planetary Science Letters, 214, 290-310.
726
727 Yaxley, G.M., and Brey, G.P. (2004) Phase relations of carbonate-bearing eclogite assemblages from
728 2.5 to 5.5 GPa: implications for petrogenesis of carbonatites. Contributions to Mineralogy and
729 Petrology, 146, 606-619.
730

731 Zha, C.S., Mibe, K., Bassett, W.A., Tschauner, O., Mao, H.K., and Hemley, R.J. (2008) P-V-T
732 equation of state of platinum to 80 GPa and 1900K from internal resitive heating/x-ray diffraction
733 measurements. Journal of Applied Physics, 103, doi: 10.1063/1.2844358.
734

FIGURE CAPTIONS

Figure 1: (a) Photograph of the experiment #21 taken whilst pressurised at ~ 80 GPa. Three (or four in the case of other experiments) ~ 40 μm sample chambers were drilled into a rhenium gasket that had been pre-indented using 200 or 250 μm diamond culets. Ruby was placed in one sample chamber only. The laser spot filled almost all of one sample chamber. ***(b)*** Illustrative cartoon showing how the temperature profiles across the heated spot change throughout each experiment. Any 'topography' in the temperature profile is maintained through the heating ramp until the melting temperature is reached, at which point the sample becomes isothermal. Further heating causes platinum migration and super-heating, generating hotspots in some experiments. If these develop, local peaks in temperature are observed that develop until the entire sample is at super-liquidus temperatures. ***(c)*** An example of the behaviour described in (b) with real data from the right-hand side of an experiment at 59.6 GPa with a melting point at 2080 ± 50 K (plateau shown in figure 4c). Even numbered profiles are shown as solid lines, odd as dashed lines. The first and last profile are labelled with the total laser power.

Figure 2: Calibration curve for pressure determination using the shift in the 1332 cm^{-1} Raman peak for diamond. The pressure measured by ruby fluorescence (one chamber in each experiment contained ruby) is plotted against the shift in Raman frequency ($\Delta\nu$ = measured Raman shift – 1332.4 cm^{-1}).

Figure 3: Three examples of temperature vs. laser power plateaux observed in enstatite-magnesite experiments and used to define eutectic melting temperatures. Temperatures marked are maximum temperatures observed within profiles measured on each side of the DAC. ***(a)*** 22.6 GPa, ***(b)*** 37.3 GPa, ***(c)*** 76.1 GPa (right hand side only used to define plateau). Open symbols show temperatures measured on the right hand side of the DAC, closed symbols are from the left hand side. The downward pointing

759 arrow marks the first observation of visible convection within the sample chamber. The error of each
760 individual temperature measurement is < 10 K. The temperatures used to define the melting
761 temperatures (grey bars) and uncertainties (2σ) are those between the two vertical black lines.
762
763 ***Figure 4:*** As figure 3, but for experiments in the magnesite-calcite system. ***(a)*** 19.6 GPa ***(b)*** 45.7 GPa
764 *(in-situ* experiment*) **(c)*** 59.6 GPa. Unlike enstatite-magnesite experiments plateaux appear short-lived,
765 due to the formation of platinum hotspots that become superheated relative to the melting temperature
766 (see text). The melting point is identified by examining individual temperature spectra in combination
767 with the presence of plateaux in temperature-power curves.
768
769 ***Figure 5*****: (a)** Melting curve for $MgSiO_3$-$MgCO_3$ system to 80 GPa. Open (ruby-bearing) and grey-
770 filled (ruby-free) circles are experiments from this study. Black squares are the eutectic melting
771 temperature at lower pressure defined in multi-anvil experiments by Katsura and Ito (1990). The
772 known transition of ilmenite to perovskite structured $MgSiO_3$ is plotted as a long dashed line (Ono *et*
773 *al.*, 2001). The melting curve is kinked at a pressure corresponding to this transition. The short dashed
774 line, open and grey squares indicates the location of the decarbonation reaction $MgSiO_3 + MgCO_3 =$
775 $Mg_2SiO_4 + CO_2$ at low pressure (Newton and Sharp, 1975; Koziol and Newton, 1998). The coefficients
776 defining the melting curve equations are presented in table 2. ***(b)*** Eutectic melting curve for the
777 $MgCO_3$-$CaCO_3$ system to 80 GPa. Open (ruby-bearing) and grey-filled (ruby-free) circles are
778 experiments from this study. The minimum melting temperature at low pressure corresponding to the
779 reaction $dolomite_{ss}$ = melt are shown as square symbols and taken from Irving and Wyllie (1975),
780 Byrnes and Wyllie (1981) and Buob *et al.* (2006). The triangular symbols represent data from Luth

781 (2001) defining the reaction dolomite$_{ss}$ = aragonite + magnesite, and this reaction has been extrapolated
782 with a dashed line. The *in-situ* experiment performed at ESRF is shown as a black diamond.
783
784 ***Figure 6:*** Field-emission gun EPMA mages of recovered products from a subsolidus (a) and
785 a partially melted (b and c) experiment. The column at the left shows backscattered electron images,
786 the centre (SiO_2) and right (MgO) columns show X-ray maps calibrated to show approximate
787 composition (in weight %) by greyscale. Labels correspond to crystalline phases: Pv = perovskite, Mag
788 = magnesite and Di = diamond and the location of the laser spot during heating is defined by a white
789 circle in (b) and (c). ***(a)*** Subsolidus experiment conducted at 33.9 ± 1.9 GPa and a maximum
790 temperature of 1950 K. Experiment consists of perovskite (with beam damage), magnesite and
791 platinum (the white phase in BSE images) of uniform grainsize evenly distributed throughout the
792 charge. ***(b)*** A surface section, adjacent to the culet, of experiment #07a conducted at 36.3 GPa. Inside
793 this heated region the grain size is significantly smaller than the surrounding material and consists of a
794 phase assemblage of MgO, perovskite and magnesite (seen in the MgO map). The colder surrounding
795 region has the same phase assemblage as (a). ***(c)*** A central section of the same experiment after further
796 polishing. In the centre of this heated region grains of SiO_2 and diamond (dark phase in BSE;
797 confirmed with Raman spectroscopy) have been identified. The central region of this experiment is
798 essentially devoid of MgO. The heterogeneity observed in (b) and (c) is a consequence of partial
799 melting and Soret diffusion in the melt (see text). The observations provide independent supporting
800 evidence for the location of the solidus and a verification of the methods used here to determine
801 melting temperatures in *in-situ* DAC experiments.
802

Figure 7: XRD data (black dots) collected at 2030K and 52.7 GPa during the *in-situ* experiment in the magnesite-calcite system and fitted using the Le Bail method (solid black curve). The background (grey dashed line) and residual (lowermost grey line) are also shown. The sample consists of the assemblage $MgCO_3$ + $CaCO_3$ in the post-aragonite structure.

Figure 8: The experimentally determined melting curves from this study for $MgSiO_3$-$MgCO_3$ and $MgCO_3$-$CaCO_3$ systems (solid black lines), with associated 95% confidence intervals (grey dotted lines), extrapolated to the pressure of the core-mantle boundary (135 GPa). The light grey field represents the Earth's adiabat from Katsura (2010) while the geotherm of a hot subducting slab is indicated by the grey arrow (Syracuse *et al.,* 2010).

Figure 9: A comparison of the melting curve of carbonated peridotite defined in a simple system ($MgSiO_3$-$MgCO_3$, this study) and in a natural carbonated peridotite system with 5 wt% CO_2 (labelled G-09, Ghosh *et al.,* 2009). Squares represent experimental runs from Ghosh *et al.* (2009); closed squares are subsolidus conditions (all carbonate as magnesite solid), open squares are experiments containing a carbonated melt and split squares are charges containing both solid and liquid carbonate. In the two experiments at 20 GPa with split symbols magnesite was only found at the cold end of the capsule estimated by the authors to be 40 – 70 °C colder than the quoted run temperature. It is suggested that the solidus of natural carbonated peridotite will also have a cusp, as observed in the simple system; a potential solidus that is consistent with the experimental data of Ghosh *et al.* (2009) is shown as a dashed curve.

Table 1: Summary of experimental results from this study

This is a preprint, the final version is subject to change, of the American Mineralogist (MSA)
Cite as Authors (Year) Title. American Mineralogist, in press.
(DOI will not work until issue is live.) DOI: http://dx.doi.org/10.2138/am.2014.4735

826

827 ***Table 1:*** Fitting parameters for the melting curves defined in this study. Polynomial equations take the

828 form $T = k_0P^2 + k_1P + k_2$. The damped Simon-Glatzel equation is $T_m = T_0\left(\frac{P}{a}+1\right)^{\frac{1}{b}}\exp(-cP)$.

fig1

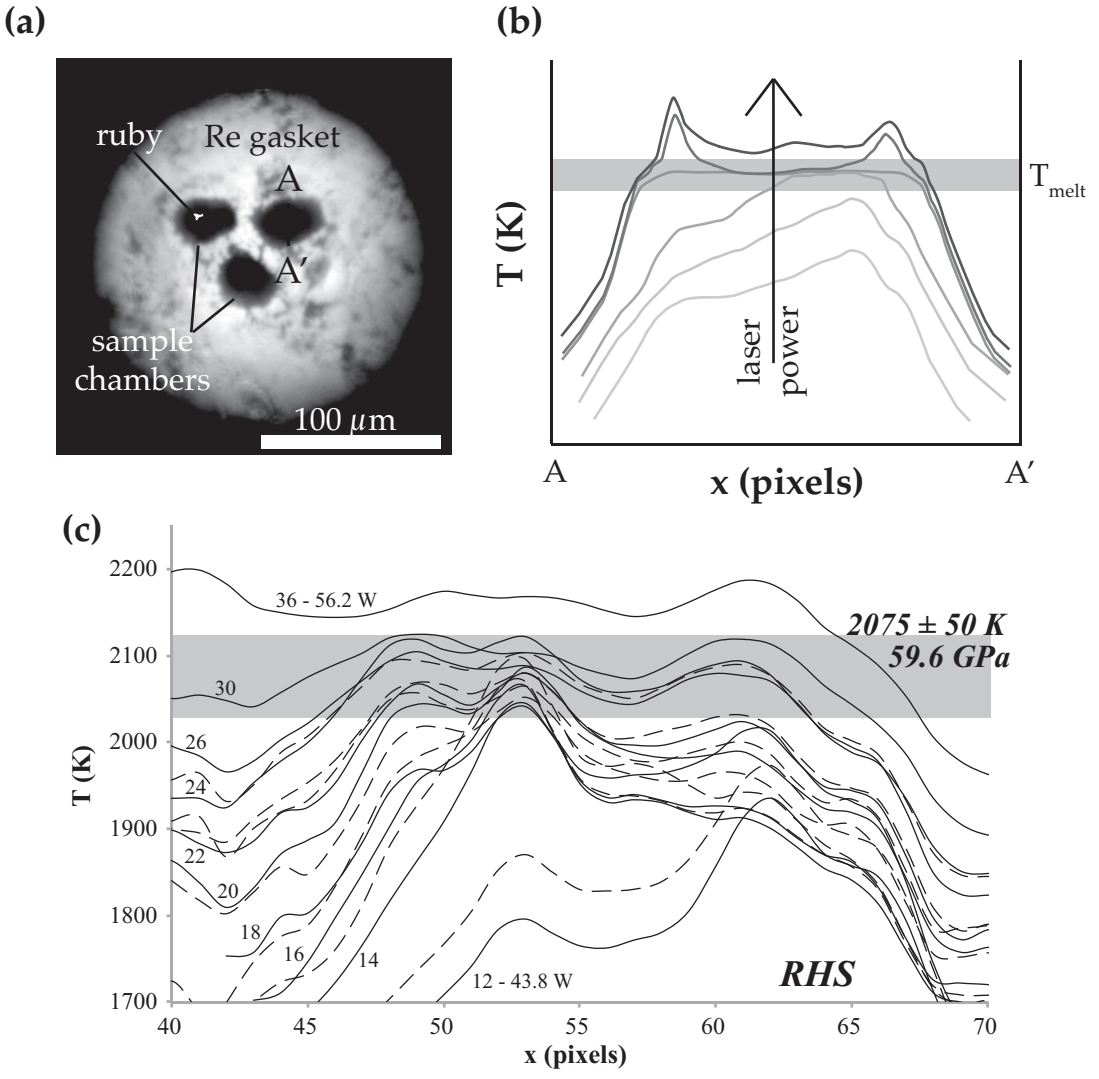
(a)
ruby
Re gasket
A
A′
sample
chambers
100 μm
(b)
T (K)
T melt
laser
power
A
x (pixels)
A′
(c)
2200
2100
2000
1900
1800
1700
T (K)
36 - 56.2 W
30
26
24
22
20
18
16
14
12 - 43.8 W
2075 ± 50 K
59.6 GPa
RHS
40
45
50
55
60
65
70
x (pixels)

fig2

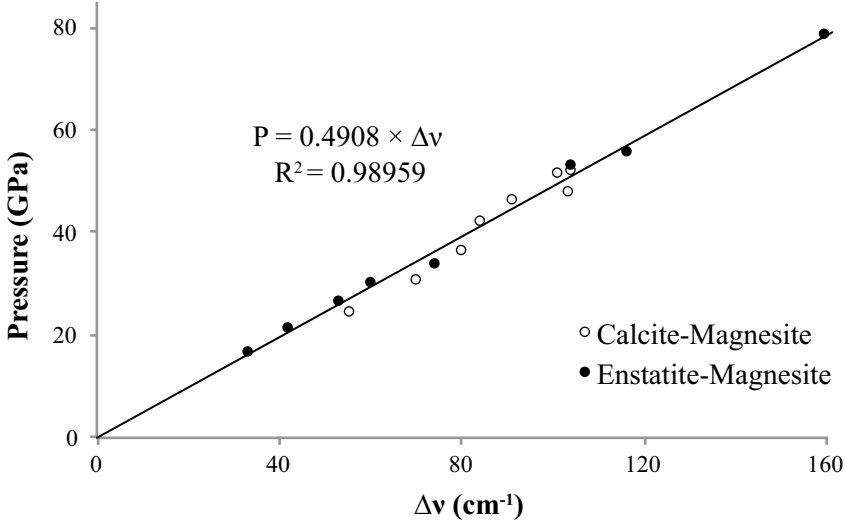
80
60
40
20
0
Pressure (GPa)
P = 0.4908 × Δν
R² = 0.98959
Calcite-Magnesite
Enstatite-Magnesite
0
40
80
120
160
Δν (cm⁻¹)

fig3

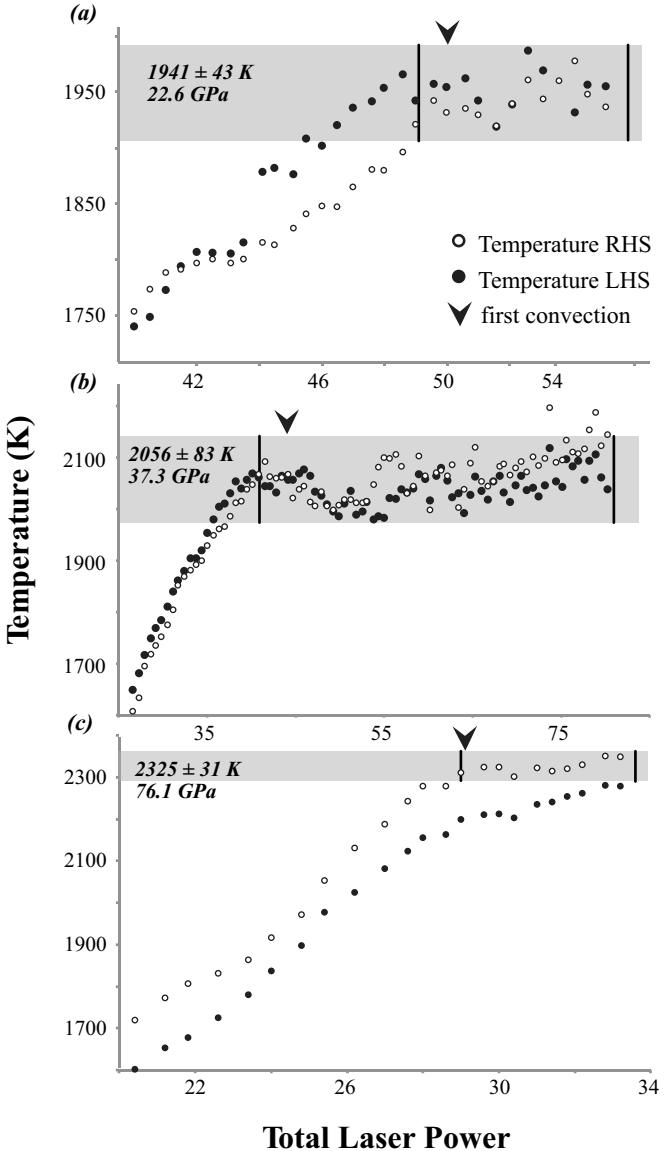
(a)
1941 ± 43 K
22.6 GPa
1950
1850
1750
Temperature RHS
Temperature LHS
first convection
42
46
50
54
(b)
2056 ± 83 K
37.3 GPa
2100
1900
1700
35
55
75
(c)
2325 ± 31 K
76.1 GPa
2300
2100
1900
1700
22
26
30
34
Temperature (K)
Total Laser Power

fig4

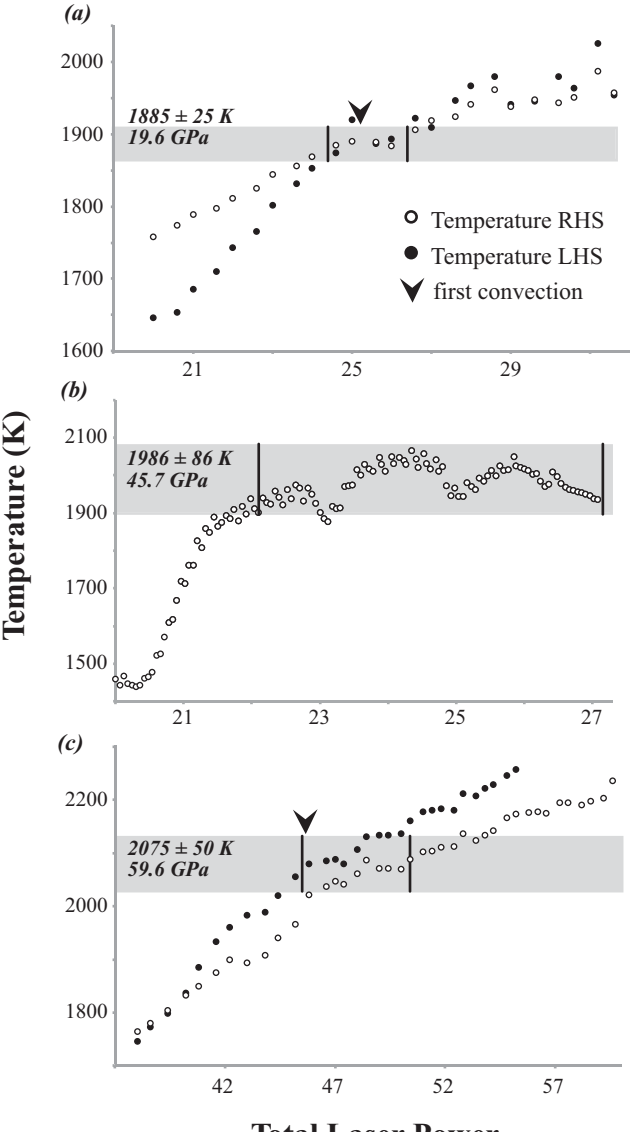
(a)
1885 ± 25 K
19.6 GPa
Temperature RHS
Temperature LHS
first convection
(b)
1986 ± 86 K
45.7 GPa
(c)
2075 ± 50 K
59.6 GPa
Temperature (K)
Total Laser Power

fig5

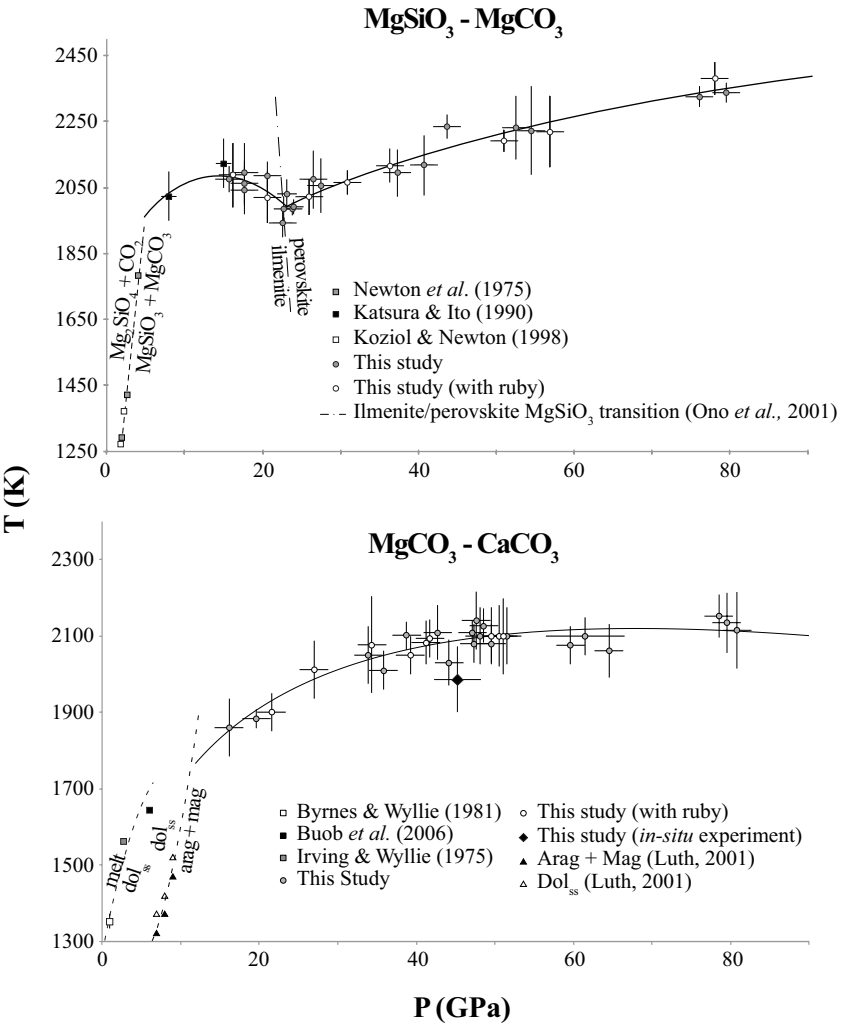
MgSiO3 - MgCO3
2450
2250
2050
1850
1650
1450
1250
0
20
40
60
80
Mg2SiO4 + CO2
MgSiO3 + MgCO3
perovskite
ilmenite
Newton et al. (1975)
Katsura & Ito (1990)
Koziol & Newton (1998)
This study
This study (with ruby)
Ilmenite/perovskite MgSiO3 transition (Ono et al., 2001)
MgCO3 - CaCO3
2300
2100
1900
1700
1500
1300
melt
dolss
dolss
arag + mag
Byrnes & Wyllie (1981)
Buob et al. (2006)
Irving & Wyllie (1975)
This Study
This study (with ruby)
This study (in-situ experiment)
Arag + Mag (Luth, 2001)
Dolss (Luth, 2001)
T (K)
P (GPa)

fig6

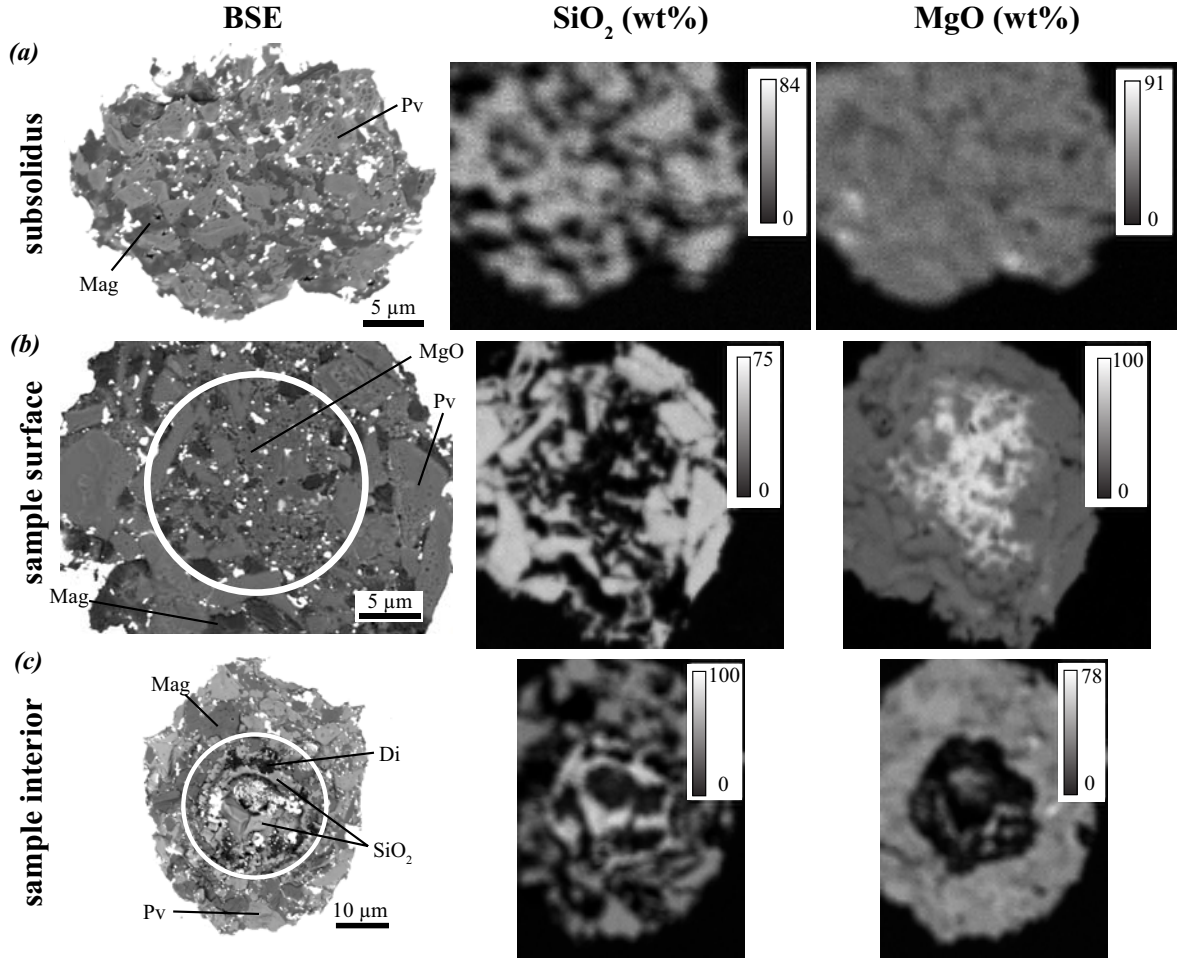
BSE
SiO2 (wt%)
MgO (wt%)
(a)
subsolidus
Pv
Mag
5 µm
84
0
91
0
(b)
sample surface
MgO
Pv
Mag
5 µm
75
0
100
0
(c)
sample interior
Mag
Di
SiO2
Pv
10 µm
100
0
78
0

fig7

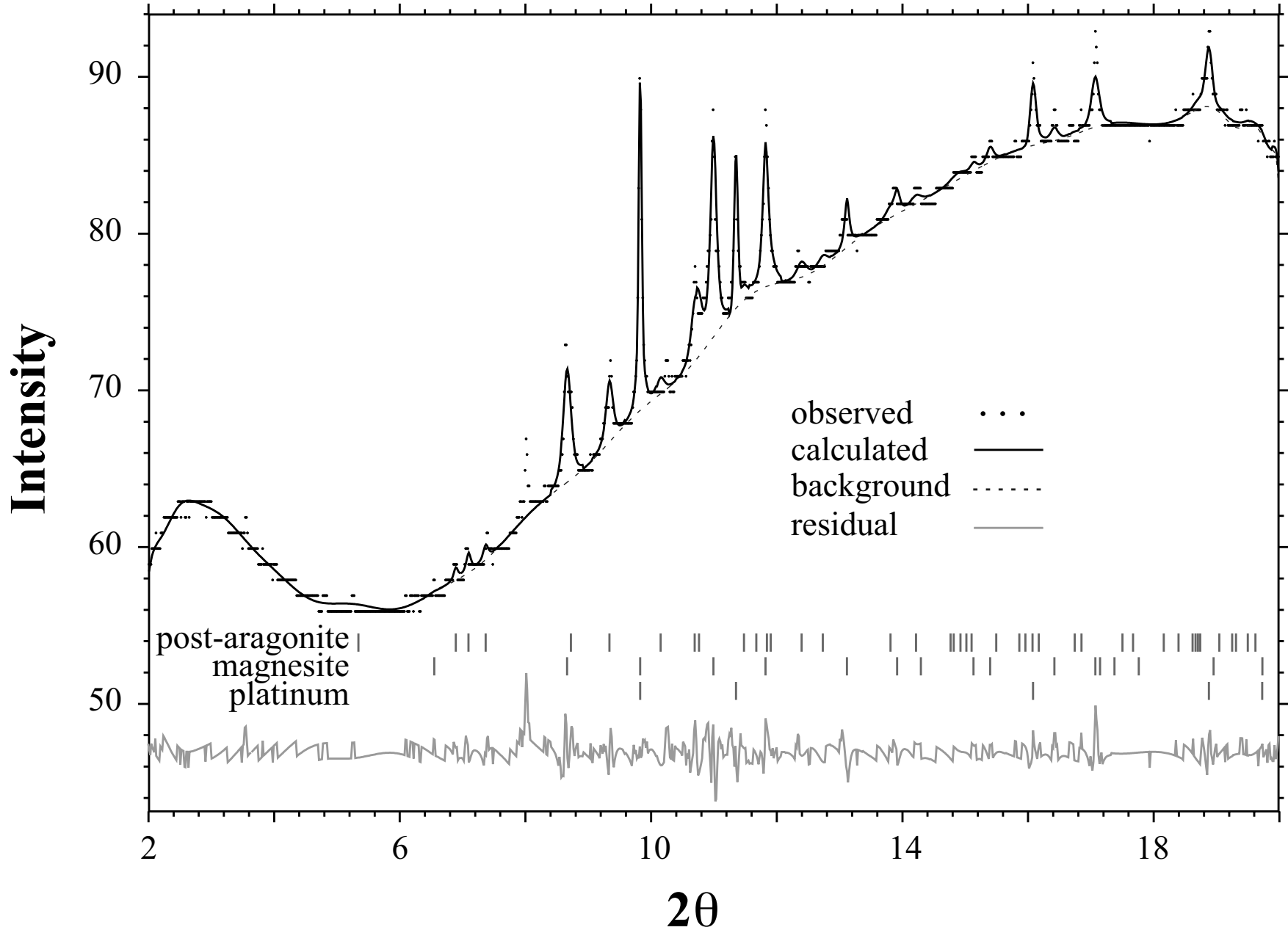
Intensity
90
80
70
60
50
2
6
10
14
18
2θ
observed
calculated
background
residual
post-aragonite
magnesite
platinum

fig8

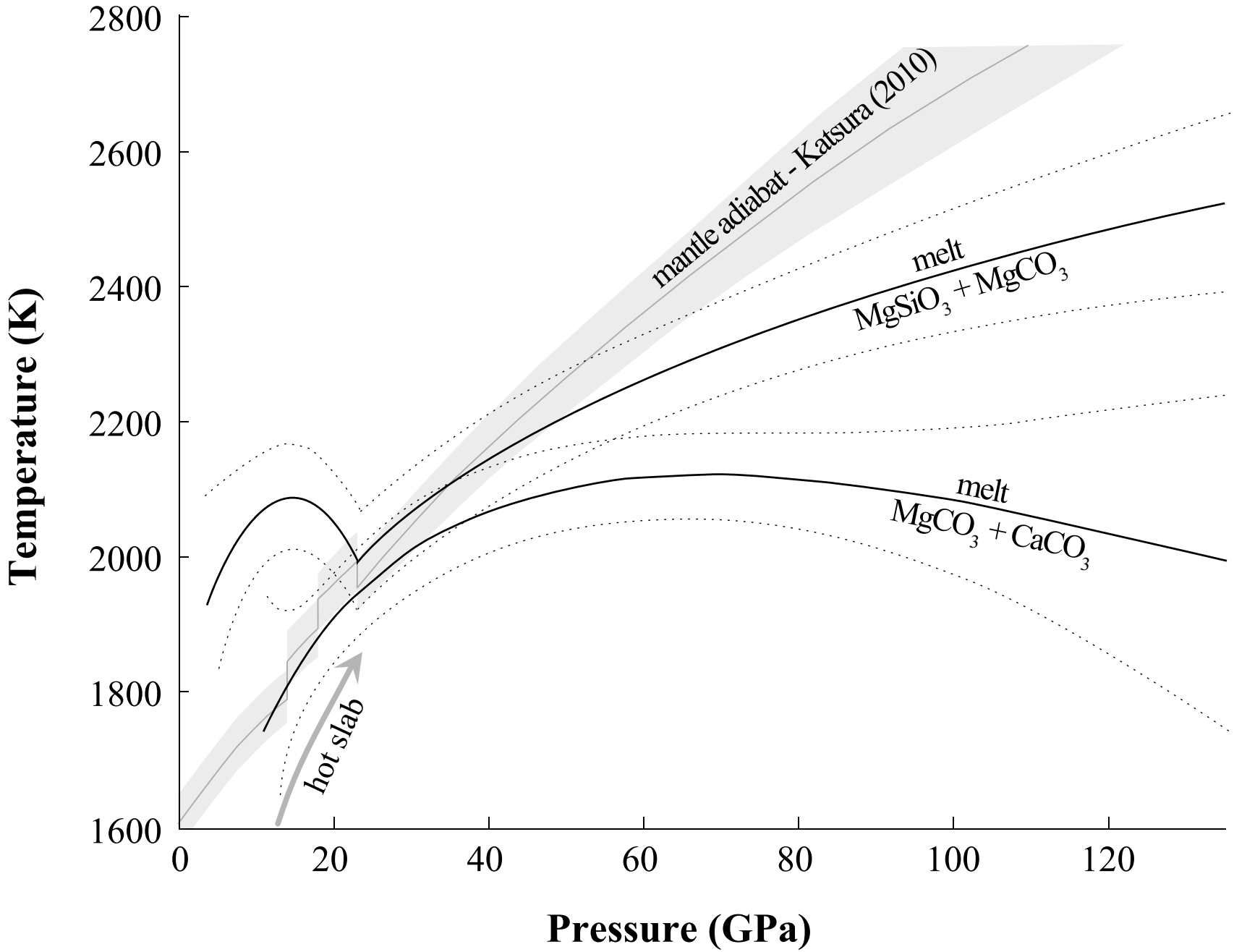
2800
2600
2400
2200
2000
1800
1600
Temperature (K)
0
20
40
60
80
100
120
Pressure (GPa)
mantle adiabat - Katsura (2010)
melt
MgSiO3 + MgCO3
melt
MgCO3 + CaCO3
hot slab

fig9

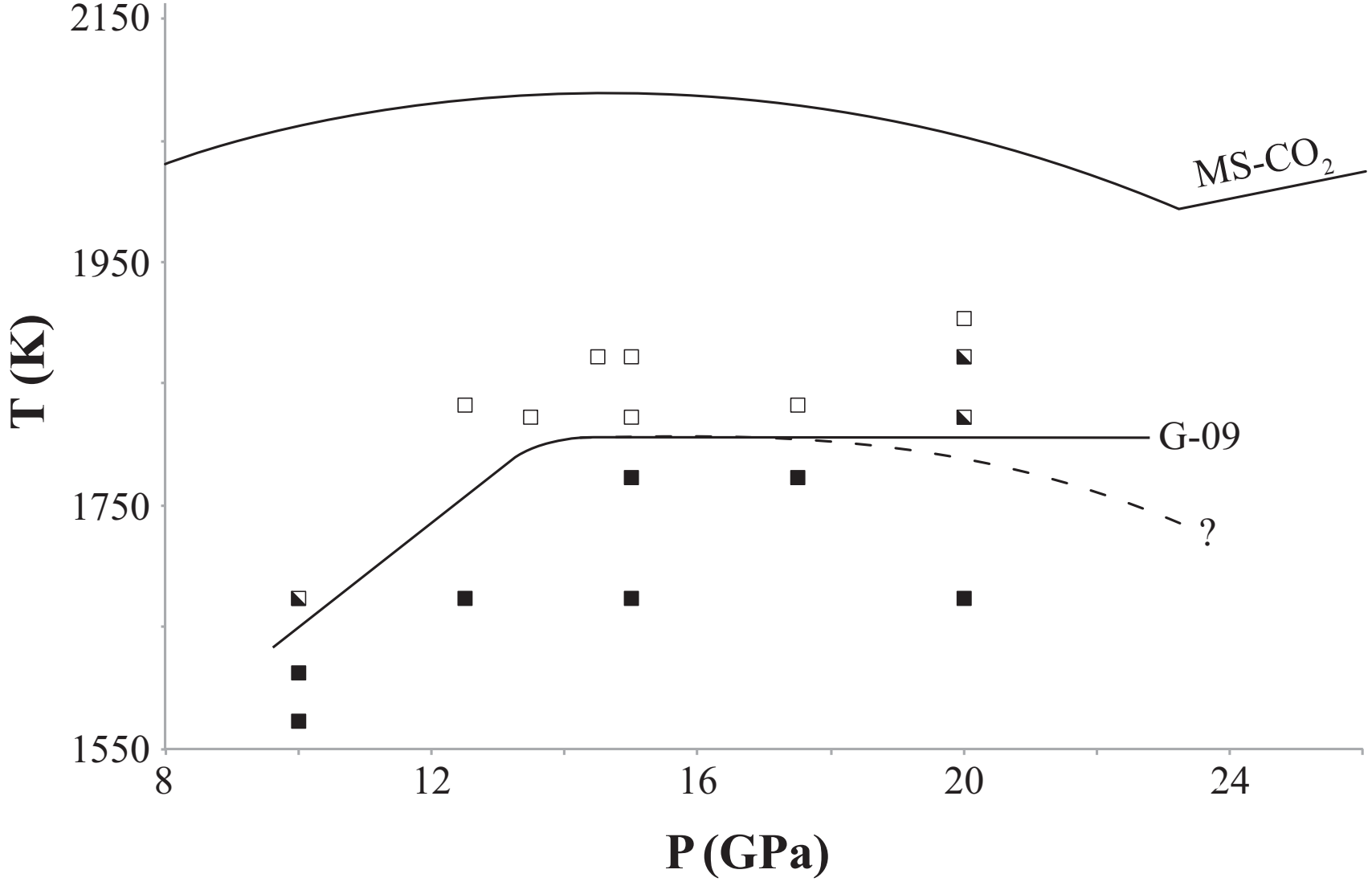

Experiment No.	Δv (cm^{-1})	P (Gpa)	T_m (K)	2σ (K)	ruby P (GPa)
MgSiO3 - MgCO3	42	20.6	2020	78	21.5
06	46	22.6	1941	43	
	36	17.7	2095	91	
	38	18.7	2050	250	
07	74	36.3	2116	51	34.1
	76	37.3	2094	72	
	56	27.5	2056	83	
09	104	51.0	2191	33	53.4
	89	43.7	2234	37	
	83	40.7	2117	91	
10	116	56.9	2219	108	56.1
	107	52.5	2230	96	
	111	54.5	2222	134	
11	33	16.2	2088	98	16.7
	36	17.7	2041	73	
	36	17.7	2063	68	
	32	15.7	2075	39	
12	53	26.0	2022	55	26.7
	54	26.5	2074	89	
	42	20.6	2086	41	
15	63	30.9	2065	36	30.5
	159	78.0	2380	50	78.5
	155	76.1	2325	31	
	162	79.5	2337	30	
20	46.4	22.8	1983	38	
	47.3	23.2	2029	44	
	48.7	23.9	1983	19.6	
	49.2	24.1	1990	22	
MgCO3 - CaCO3	80	39.3	2050	50	36.42
02	90	44.2	2030	60	
	73	35.8	2010	50	
03	101	49.6	2100	75	51.71
	101	49.6	2080	50	
	96.5	47.4	2080	50	
13	44	21.6	1900	50	
	40	19.6	1885	25	
	33	16.2	1860	75	
14	55	27.0	2012	76	24.6
	70	34.4	2077	126	31.1
	69	33.9	2050	75	
	87	42.7	2109	71	
16	84	42.1	2083	58	42.3
	97	47.6	2141	76	
	99	48.6	2127	44	
17	103	50.6	2100	80	48.1
	-	*61.5*	2100	50	
	131.5	64.5	2060	50	
	121.5	59.6	2075	50	
18	104	51.0	2100	100	52.4
	98	48.1	2100	75	
	105	51.5	2100	75	
19	85	41.7	2094	50	46.7
	96	47.1	2109	32	
	79	38.8	2101	37	
21	159.9	78.5	2151	56	
	164.6	80.8	2114	100	
	161.9	79.5	2134	39.5	
In-situ experiment	N/A	45.7*	1986	86	

*post-heating pressure from Pt MGD EoS (Zha *et al.,* 2008)

$MgSiO_3$ - $MgCO_3$	k_0	k_1	k_2	
5-23 GPa	-1.305	38.32	1806	
±	*0.7976*	*27.56*	*231*	
	T_m^0	**a**	**b**	**c**
> 23 GPa	1039	0.1848	7.44	0
±	*2.06E+04*	*28.1152*	*5.32*	*0*
$MgCO_3$ - $CaCO_3$	T_m^0	**a**	**b**	**c**
> 12 GPa	994.05	0.67003	4.8058	0.00303
±	*1.08E+04*	*40.8*	*10.58*	*0.00542*